Green Chemistry

PAPER

View Article Online
View Journal | View Issue

Cite this: *Green Chem.*, 2024, **26**, 8020

Synthesis of highly dispersed carbon-encapsulated Ru–FeNi nanocatalysts by a lignin–metal supramolecular framework strategy for durable water-splitting electrocatalysis†

Jianglin Liu, [a] Xueqing Qiu, *[a,b,c] Shirong Sun, *[a] Bowen Liu,[a] Yuhui Tian,[a] Yanlin Qin [a,b,c] and Xuliang Lin *[a,b,c]

The utilization of plant polyphenols as catalyst carriers holds promise for environmentally friendly catalysis. However, challenges such as the inhomogeneous distribution of organic ligands often hinder their effectiveness. In this study, lignin–metal supramolecular framework were formed through ionic coordination self-assembly, achieved by oxidative ammonolysis modified lignin. The specific spatial domain-limiting effect of lignin–metal supramolecular framework ensures the dispersion and stability of catalyst active sites. Carbon-coated trimetallic catalysts (Ru–FeNi@OALC) derived from lignin–metal supramolecules exhibit promising performance, with low overpotentials for the oxygen evolution reaction (OER, η_{10} = 290 mV) and the hydrogen evolution reaction (HER, η_{10} = 52 mV), surpassing commercial noble metal catalysts. Additionally, these catalysts demonstrate long-lasting water-splitting performance, highlighting their potential for sustainable catalytic reactions. Molecular simulations and DFT theoretical calculations elucidate the feasibility of lignin oxidative ammonolysis modification and reveal the coordination mechanism. Furthermore, the abundant defects and disorder in the coordination polymer-derived carbon materials optimize electron transfer processes and accelerate reaction kinetics. This construction strategy towards designable polyphenol–metal supramolecular framework presents a promising avenue for the green synthesis of a variety of metal/carbon composite catalysts, contributing to sustainable catalysis and environmental protection.

Received 11th April 2024,
Accepted 4th June 2024

DOI: 10.1039/d4gc01788a

rsc.li/greenchem

1 Introduction

The rapid development of state-of-the-art carbon-based metal electrocatalysts has played a great role in improving catalysis of the oxygen evolution reaction (OER),[1] the hydrogen evolution reaction (HER),[2] and the oxygen reduction reaction (ORR) for energy conversion and storage due to their special properties,[3–6] including excellent chemical and mechanical dependability,[7] tunable porosity and surface properties,[6] good electrical and thermal conductivity,[8] large specific surface area,[9] variable structural and morphological combinations,[10] easy handling,[11] and low production cost.[11] Although carbon-based metal electrocatalysts of various metal elements have been prepared using predesigned substrates (*e.g.*, graphene,[12] carbon nanotubes,[13] g-C_3N_4,[14] and carbon black[15]), the generation of catalytic sites is highly dependent on the structure of the substrates and the synthesis methods, which are challenging when preparing different materials.

Supramolecular complexation is a powerful strategy that takes advantage of the assembly of metal species and organic ligands at the molecular level resulting in the formation of metals confined in the support matrix.[16–18] Therefore, these methods are usually applied to produce catalysts with one specific material and it remains challenging to form hybrids with other foreign substrates.[19,20] Polyphenols are currently well-studied candidates for supramolecular complexation, but due to metal aggregation that is easily caused under high-temperature pyrolysis, supramolecular complexes must be loaded on other substrates for catalyst preparation.[21–23] In addition, the catalytic stability and material cost of polyphenol-based carbons are still the limiting factors for their industrial application.[24,25] There is an urgent need to develop a ver-

[a]*Guangdong Provincial Key Laboratory of Plant Resources Biorefinery, School of Chemical Engineering and Light Industry, Guangdong University of Technology, Guangzhou 510006, China. E-mail: cexqqiu@scut.edu.cn, shirongsun@gdut.edu.cn, xllin@gdut.edu.cn*

[b]*Guangdong Provincial Laboratory of Chemistry and Fine Chemical Engineering Jieyang Center, Jieyang 515200, China*

[c]*Guangdong Basic Research Center of Excellence for Ecological Security and Green Development, Guangdong University of Technology, Guangzhou 510006, China*

† Electronic supplementary information (ESI) available. See DOI: https://doi.org/10.1039/d4gc01788a

satile and economic supramolecular complexation precursor that can be flexibly adjusted to meet the needs of rapidly developing applications.[26,27]

Lignin, a highly abundant natural aromatic polymer, is derived from the radical polymerization of three phenyl propylene precursors, *i.e.*, *p*-coumaryl (4-hydroxycinnamyl), coniferyl (4-hydroxy-3-methoxylcinnamyl), and sinapyl (4-hydroxy-3,5-dimethoxycinnamyl) alcohols.[28,29] The C–O bonds (β-O-4, α-O-4, α-O-γ and 4-O-5) and C–C bonds (β-5, β–β, β-1 and 5–5) between these three structural units, the π–π conjugation between aromatic nuclei and the hydrogen bonding between hydroxyl groups constitute the intricate three-dimensional network structure of lignin (Fig. S1†).[30–34] Although the heterogeneous and complex structural characteristics of the lignin polymer make it difficult to develop lignin for high-value applications,[35–38] the abundance of hydroxyl groups and aromatic rings enables lignin to be easily modified through covalent and non-covalent interactions.[39–43] Moreover, lignin can trap and coordinate metal ions *via* these abundant hydroxyl groups and diverse modification sites to self-assemble into complexes with well-defined surface chemistry and morphology,[44–50] which have great potential in catalyst applications. Therefore, lignin appears to be a plausible candidate for industrial-scale low-cost carbon supports for the construction of metal–organic precursors, while it is currently largely destined for combustion.[51–54]

Herein, we take advantage of lignin's organic chemistry and report a localized lignin–metal supramolecular framework strategy for the preparation of highly dispersed carbon-encapsulated metal catalysts for durable water splitting electrocatalysis, as shown in Fig. 1. An appropriate amount of amide groups as coordination sites was introduced into technical lignin through a partial ring-opening oxidative ammonolysis modification reaction. After chelating with metals (Fe^{3+}, Ni^{2+} and Ru^{3+}) according to their own growth pattern, the formed supramolecular complexes are then subjected to pyrolysis to decompose the precursor ligands, resulting in the formation of carbon-encapsulated Ru–FeNi catalysts with excellent high dispersity.[50] We systematically describe the process of oxidative ammonolysis of lignin and reveal its coordination mechanism with transition metal ions and the spatial limiting effect of this on the formation of highly dispersed nanoparticles. The highly dispersed lignin-derived carbon nanoparticles were used to electrocatalyze the water decomposition reaction, which paves the way for their further application.

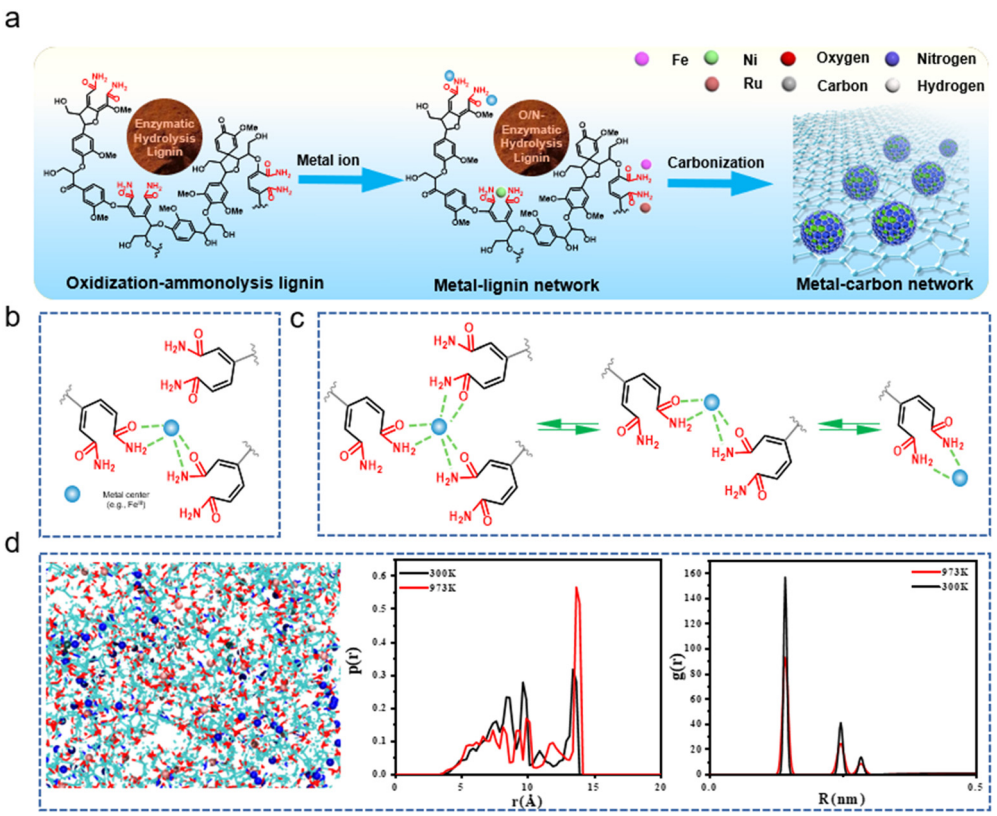

Fig. 1 (a–c) Schematic illustration of the synthesis route to rational highly dispersed carbon-encapsulated metal catalysts using lignin as the only carbon source. Lignin was first converted into water-soluble biomolecules rich in acylamino groups. This product is then directly mixed with metal salts to produce metal–lignin supramolecular framework, which are then carbonized to prepare carbon-encapsulated metal catalysts. (d) Representative configuration of OAL-M in the simulation studied and plots of the probability distribution function ($p(r)$) of pore size and the aromatic ring–ring radial distribution function ($g(r)$) in OAL-M upon heat treatment at different temperatures.

2 Experimental section

2.1 Materials and chemicals

Enzymatic hydrolysis lignin (EHL) was kindly provided by Shandong Longlive Bio-Technology Co., Ltd. Hydrogen peroxide solution (30 wt% in H_2O), ammonia solution (25 wt% in H_2O) and DMSO-d_6 (99.9% + 0.03% TMS) were purchased from Shanghai Macklin Biochemical Co., Ltd. Iron chloride hexahydrate ($FeCl_3{\cdot}6H_2O$, AR, 99%), nickel chloride ($NiCl_2{\cdot}6H_2O$, AR, 99%), ruthenium chloride ($RuCl_3{\cdot}xH_2O$), ethanol (C_2H_5OH, AR, 99.7%), commercial platinum carbon (20 wt%), and ruthenium carbon were provided by Shanghai Aladdin Chemical Co., Ltd. Hydrochloric acid (HCl, 36.0%–37.0%), nitric acid (HNO_3, 65.0%–68.0%), sodium hydroxide (NaOH, AR, 96%), and potassium hydroxide (KOH, AR, 85%) were purchased from Guangzhou Chemical Reagent Factory. Nafion solution (D520, 5 wt%) was supplied by DuPont. All reagents used in this study were commercially purchased and used as received. Carbon paper (TGP-H-060, 20 × 20 cm, 0.19 mm) was produced by the Toray Corporation (Japan). Deionized water (DIW) was used throughout all experiments.

2.2 Process of oxidative ammonolysis modified lignin

In a typical process of oxidative ammonolysis modified lignin (OAL), 10 g of EHL was dispersed in 90 mL of 3% ammonia solution, then 10 mL of 30% hydrogen peroxide was added, and the mixture was stirred at room temperature for 10 min. Afterwards, the mixture was transferred into a hydrothermal reactor and reacted at 120 °C for 90 min. After the reaction, the mixture was cooled to room temperature. The reaction product (OAL) was subjected to rotary evaporation to remove unreacted reactants and water and then vacuum-dried and ground into powder.

2.3 Preparation of the localized lignin–metal supramolecular framework and Ru–FeNi@OALC catalysts

OAL (1.0 g) was dispersed in 100 mL of deionized water, while $FeCl_3{\cdot}6H_2O$ (0.129 g), $NiCl_2{\cdot}6H_2O$ (0.113 g), and $RuCl_3{\cdot}xH_2O$ (0.010 g) were vigorously stirred into 50 mL of pure water. This mixture was added dropwise into the aqueous dispersion of OAL and stirred for 1 h. The precipitate was centrifuged, washed with ultrapure water, vacuum dried at 40 °C for 24 h, and subsequently pulverized to obtain OAL–metal composites after aging for 12 h. The precursor material (1.0 g) was evenly ground and was first insulated at 25 °C for 0.5 h under an N_2 atmosphere in a tube furnace. Then, it was heated to 700 °C at a heating rate of 5 °C min^{-1}, insulated at 700 °C for 2 h, and finally cooled to 20–30 °C. The synthesized product was washed with deionized water and 1 mol L^{-1} HCl repeatedly and dried in a vacuum oven overnight. The Ru@OALC and FeNi@OALC were prepared *via* similar procedures.

3 Results and discussion

In order to verify the occurrence of the coordination process, we first studied the molecular dynamics (MD) of OAL-M at different temperatures by calculating the supramolecular structure of OAL-M (Fig. 1d). After applying heat to the model system, the OAL-M underwent thermodynamic delocalization in a confined space to simulate the motion of interrelated OAL-M. The probability distribution curve of these interrelated OAL-M revealed their different thermodynamic behaviors at different temperatures, namely 300 K (room temperature) and 973 K. At 300 K, the radial distance of the MPN cluster was 13.7 Å, and at 973 K, the radial distance of the MPN cluster was 14.1 Å, which indicated that the local structure of the MPN cluster could be adjusted by heating. In addition, MD simulations revealed aromatic ring–ring fillers through the radial distribution function $g(r)$. At 300 K and 973 K, the main spacing value of aromatic ring-to-ring packing did not change, only the strength changed. With the increase in temperature, the radial distribution intensity decreased, and the benzene inter-ring force decreased.

The main information on the EHL and the modified lignin (OAL) structures, including the distribution of various inter-unit linkage types, aromatic nucleus types and modified structures, was analyzed using the 2D HSQC NMR method, which is particularly valuable for identifying the structure of lignin (Fig. 2). For EHL that contains mainly β-O-4 and β-5 linkages and no β–β linkage (Fig. 2a), we reasoned that the β–β-linked units should be broken during the enzymatic hydrolysis and alkali post-treatment processes. Among these linkages, the β-O-4 linkage constitutes a high content indicating that the EHL used in this study is representative of conventional industrial lignin. Additionally, three aromatic nuclei units, namely, *p*-hydroxyphenyl (H), guaiacyl (G), and syringyl (S), were clearly shown in the aromatic region of the NMR spectrum for EHL run in DMSO-d_6 (Fig. 2c). In the regions of δ_H/δ_C = 7.4–7.7/130–132 and 6.2–6.5/115–118 ppm, two C–H correlation clusters were assigned to the structures of *p*-coumarate (*p*CA) and ferulate (FA), which are typical structures found in natural lignin from corncob. Detailed information on the OAL structures is shown in Fig. 2b and d. It is clear that the correlations for OAL are quite different from those of EHL. Almost all the β-5 linkages and a portion of the β-O-4 linkages were oxidized and broken, while some of the β-O-4-S linkages were retained in the OAL, which indicated that lignin containing a large number of S nuclei can resist oxidative cleavage of its side chains during modification by the oxidative ammonolysis reaction. This may be due to the readily occurring electron transfer after the oxidation of the G-nucleus, making it more prone to Cα–Cβ cleavage.[55,56] One of the most intriguing observations came from comparing data from the aromatic regions (Fig. 2c and d) which showed three oxidative ammonolysis structures (GBa, pBa and Hda) with relatively suitable content for subsequent coordination reactions with metals. As the results showed (Fig. 2d), sufficient evidence proved that the Hda structure (δ_H/δ_C = 6.2–6.3/119–121, 6.3–6.4/122–123 and 7.8–7.9/131–132 ppm) was introduced by the oxidative ring-opening reaction of lignin. Its ring-opening amount accounted for 18.1% of the total aromatic ring content. Besides, two structures of benzamide derivatives (GBa and pBa) provided more

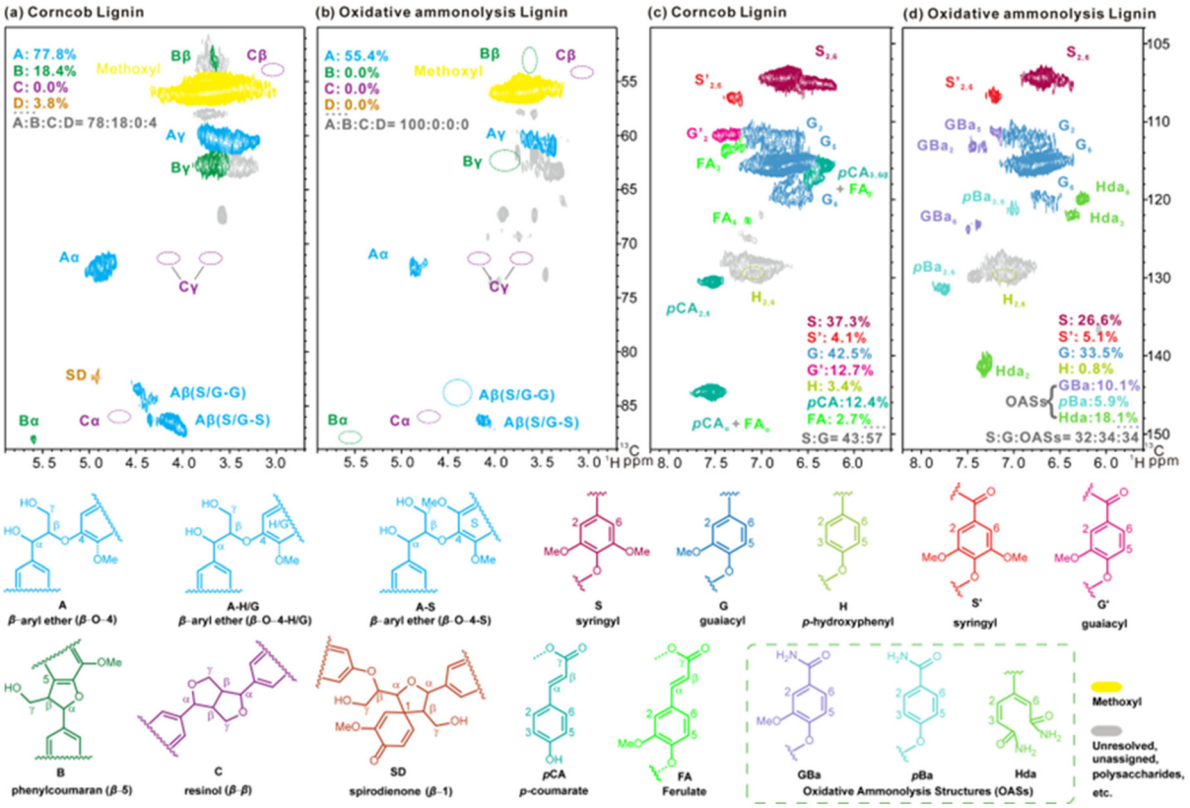

Fig. 2 Partial 2D HSQC NMR spectra of corncob lignin (in DMSO-d_6) before and after modification by oxidative ammonolysis. The aliphatic region (a) and aromatic region (c) of corncob lignin were mentioned in previous work.[57] The aliphatic region (b) and aromatic region (d) correspond to the oxidative ammonolysis-modified lignin. Contours are color coded to the responsible structures. Percentages are from volume integrals; pCA and FA are reported on an S + G basis.

coordination sites. The ^{1}H and ^{13}C ChemNMR estimations of the structures of GBa, pBa and Hda are listed in the ESI (Fig. S2 and Tables S1–6†). The evidence shows that the modified method was appropriate, the main structure of lignin was preserved, and no additional metal ions were introduced.

The lignin–metal supramolecular framework was simply obtained by mixing OAL with metal salts using water as solvent. The FTIR spectra of EHL, OAL, and OAL-M are shown in Fig. 3a. Compared with the FTIR spectrum of EHL, a new peak appeared at 1351 cm^{-1} in the FTIR spectrum of OAL that corresponds to the stretching vibrations of –CO-NH_2. The decrease in the peak value of the phenylpropane structure at 1410, 1551, and 1607 cm^{-1} indicated partial cracking of the aromatic ring. Then, due to the interaction between metal ions and –CO-NH_2, this peak disappeared in the OAL-M supramolecular framework. This result demonstrated the coordination between OAL and metal ions and the formation of a lignin–metal supramolecular framework. The same conclusion was supported by ^{13}C solid-state NMR (Fig. S3†). The UV-visible absorption spectrum of the OAL-M supramolecular framework showed the characteristic ligand-to-metal charge-transfer (LMCT) band of OAL-Fe^{3+} coordination at $\lambda \approx 385$ nm (Fig. 3b). Conversely, OAL and Fe^{3+} solutions were featureless in the same spectral region (350–550 nm). The XPS spectra of OAL and the OAL-M supramolecular framework (M = Fe^{3+}, Ni^{2+}, and Ru^{2+}) are shown in Fig. 3c–f. In the O 1s spectrum of OAL (Fig. 3c), two peaks at 533.01 eV and 531.52 eV are attributed to the C–O–C, C–O–H, Ph–O–Ph, Ph–O–C, and C═O, respectively. As shown in Fig. 3d, for OAL-M, the C–O–M content increased relative to that of OAL, indicating coordination of OAL and metal ions on the OAL-M supramolecular framework during simple mixing. The Fe 2p, Ni 2p, and Ru 2p XPS spectra indicated that some of the metal ions were reduced during the formation of supramolecules, further proving the interaction between lignin and metals (Fig. S4†). In Fig. 3f, the N 1s spectrum of OAL-M showed a new peak (M–N) at 399.71 eV with content of 25.53% compared with that of OAL (Fig. 3e), which was in accordance with the results of the FTIR analysis (Fig. S5†). In addition, according to the radial distribution diagram and coordination number of metal and O and N coordination, it could be seen that the coordination number of the ligand was related to the feed ratio. With the increase of metal content, its coordination number increased and gradually stabilized.

The characteristics of pristine Ru–FeNi@OALC were investigated. Transmission electron microscopy (TEM) provided a detailed view of the morphology, revealing densely packed nanosheets (Fig. S6a†). Fig. 4a displays a high-magnification

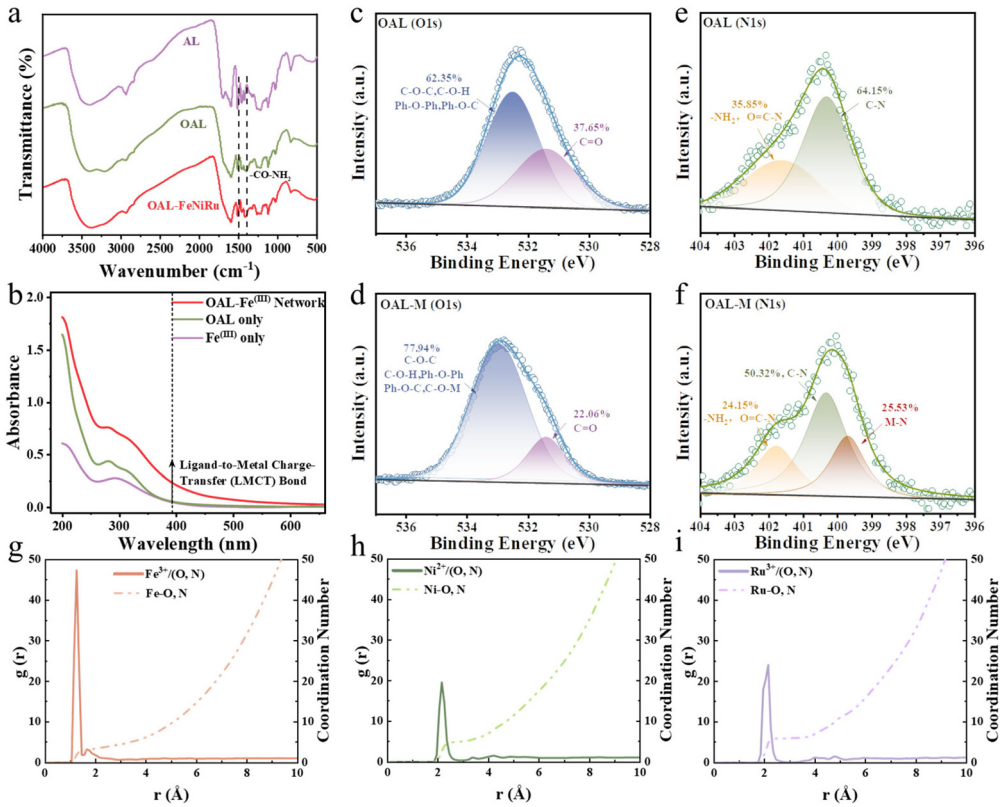

Fig. 3 Characterization and properties of the OAL-M supramolecular framework. (a) FTIR spectra of AL, OAL, and OAL-M supramolecular framework. (b) UV/visible absorption spectrum of an OAL-M supramolecular framework. Absorption spectra of OAL and Fe^{III} solutions are also shown. (c and d) O 1s XPS spectra of dried OAL and OAL-M gels. (e and f) N 1s XPS spectra of dried OAL and OAL-M gels. (g–i) Radial distribution and coordination number of Fe, Ni and Ru and O and N coordination, respectively.

TEM image showing uniformly distributed nanoparticles of similar sizes across the entire nanosheet surface, resulting in high surface roughness conducive to exposing more active sites and enhancing reaction kinetics by eliminating bubbles. In contrast to carboxymethylated lignin, lignin from oxidative ammonolysis yielded a catalyst with more complex sites, and the spatial confinement of the organic molecular framework facilitated the high dispersion of Fe, Ni, and Ru atoms within the lamellar structure, as confirmed by TEM coupled with EDS element mapping (Fig. 4b). The formation of Ru–FeNi@OALC involved nanoparticles being embedded within a lignin-derived carbon matrix. Statistical analysis (Fig. 4c) revealed nanoparticle sizes ranging from 1 to 15 nm, with an average size of 5.7 nm. The lignin carbon layer effectively prevented nanoparticle agglomeration during mosaic structure formation, leading to increased material surface area and catalytically active sites. A high-resolution transmission electron microscopy (HRTEM) image (Fig. 4d) reveals nearly regular spherical nanoparticles (~10 nm) surrounded by the lignin-derived carbon layer. Singularly dispersed FeNi alloys and Ru nanoparticles were abundantly observed on Ru–FeNi@OALC, with interplanar spacings corresponding to the (101) plane of FeNi alloys and the (100) plane of Ru nanoparticles, respectively. During the carbonation process, tiny FeNi alloy and Ru clusters epitaxially grew on lignin-derived carbon nanosheets, forming strongly coupled heterointerfaces. The poly-crystalline structure of Ru–FeNi@OALC was evident from the selected area electron diffraction (SAED) pattern (Fig. 4e), with diffraction rings corresponding to the (102), (101), and (100) planes of Ru nanoparticles, respectively.

The chemical constituents of the Ru–FeNi@OALC composite were further characterized by X-ray diffraction (XRD) spectroscopy. As displayed in Fig. 4f, the signal at $2\theta = 26°$ could be ascribed to the (002) plane of graphitic carbon, and the broadness of this peak indicated the ultrathin thickness of the graphene-like carbon shells. Moreover, all the diffraction peaks could be well indexed into the standard PDF cards of Ru (JCPDF #88-1734) and FeNi alloy (JCPDF #47-1417), which was consistent with the above TEM results, further confirming that the Ru/FeNi heterojunction was formed successfully. To further analyze the elemental components and chemical states of these samples, X-ray photoelectron spectroscopy (XPS) was conducted. As displayed in Fig. S7a,† the survey-scan spectrum manifested that the sample was composed of Fe, Ni, Ru, C, and N elements. The C 1s spectrum confirmed the existence of C–C (284.8 eV), C–N (285.4 eV), C–O (286.7 eV), and C═O (288.8 eV) in Ru–FeNi@OALC (Fig. S7b†). The C–N bond indicated that N was successfully doped into the carbon skeleton,

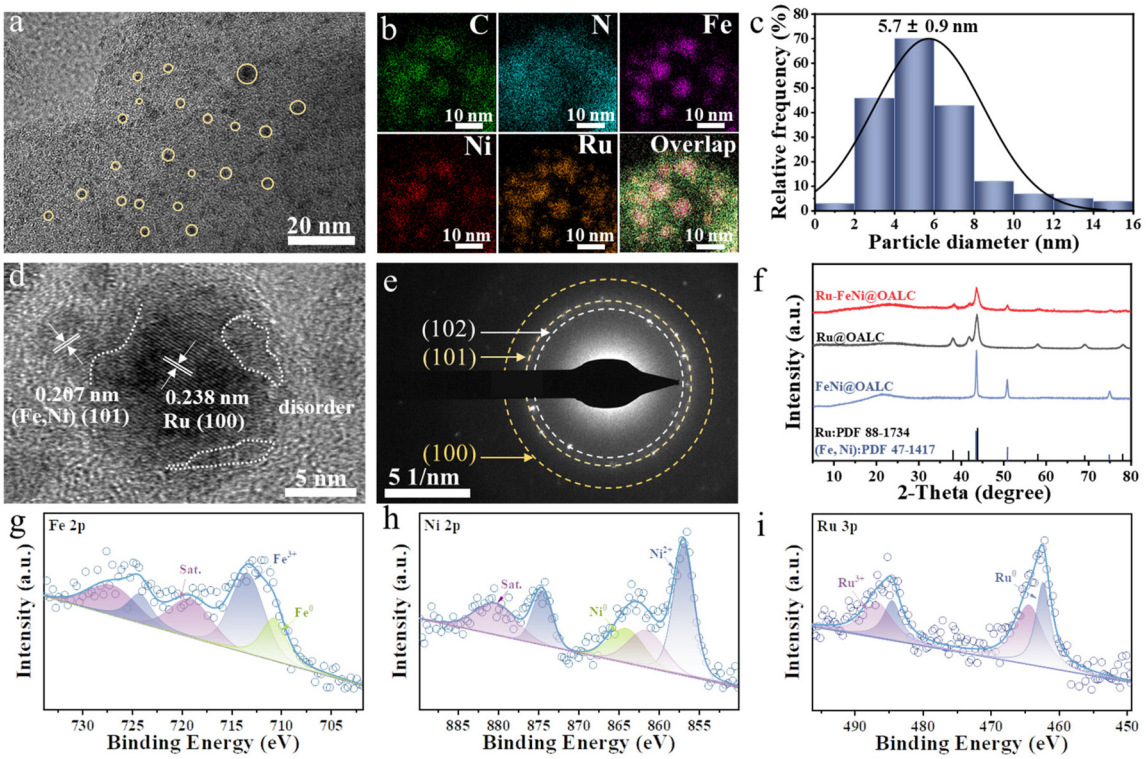

Fig. 4 Characterization of the Ru–FeNi@OALC catalyst. (a) TEM image. (b) HAADF-STEM image and corresponding EDS mappings. (c) Particle diameter dispersity. (d) HRTEM image. (e) Selected area electron diffraction (SAED) image. (f) XRD patterns of Ru–FeNi@OALC, Ru@OALC and Ru@OALC catalysts. (g) Fe 2p XPS spectrum of Ru–FeNi@OALC. (h) Ni 2p XPS spectrum of Ru–FeNi@OALC. (i) Ru 3p XPS spectrum of Ru–FeNi@OALC.

whereas C═O implied that substantial oxygen-containing groups were decorated on the surface, potentially creating defects in the carbon matrix. The high-resolution N 1s spectrum (Fig. S7c†) could be well fitted into three peaks and assigned to pyrrolic N (398.6 eV), graphitic N (400.9 eV), and oxidized N (404.3 eV), respectively. The incorporation of N into lignin-derived carbon nanosheets could not only effectively enhance the overall electrical conductivity of carbon nanosheets but also generate some defects or vacancies among carbon nanosheets, therefore affording numerous active sites for electrocatalysis and thus expediting the reaction kinetics.[58] As for the deconvoluted spectrum of the Fe 2p state for Ru–FeNi@OALC, the doublet peaks at 713.4 and 724.2 eV were attributed to Fe^{3+}, along with two doublet satellites (Fig. 4g). Besides, the shoulder peak at 710.7 eV arose from Fe0. As shown in the Ni 2p spectra in Fig. 4h, the peak located at 864 eV was ascribed to the Ni $2p_{3/2}$ of Ni^0. The peaks centred at 856.9 and 874.5 eV (Ni $2p_{3/2}$ and Ni $2p_{1/2}$ of Ni^{2+}) indicated the partial oxidation of the surface Ni atoms, and the remaining two peaks were their corresponding satellite peaks. Moreover, the Ru 3p spectrum of Ru–FeNi@OALC revealed that the dominant couple of peaks at 462.3 and 484.5 eV corresponded to Ru^0. In contrast, the other two peaks at 464.4 and 486.7 eV were assigned to Ru^{3+} due to partial surface oxidation (Fig. 4i). The exact contents of Fe, Ni and Ru were determined by inductively coupled plasma emission spectrometry (ICP-OES) to be 3.2 wt%, 1.3 wt% and 8.6 wt%, respectively. Noteworthily, relative to FeNi@OALC, the positive peak shifts of the Fe 2p and Ni 2p states could be observed in Ru–FeNi@OALC, heralding the beneficial electron transfer and charge density redistribution upon the as-obtained heterointerfaces, in line with the electronegativity trend and theoretical results.

The electrocatalytic HER activities of Ru–FeNi@OALC were investigated using linear sweep voltammetry in 1.0 M KOH (Fig. 5a). Ru–FeNi@OALC reached a current density of 10 mA cm^{-2} at an extremely low overpotential of 52 mV, while Ru@OALC, FeNi@OALC, and commercial Pt/C required relatively high overpotentials of 93, 460, and 40 mV, respectively. Fig. 5b shows the Tafel plots of the catalysts. Ru–FeNi@OALC possesses a Tafel slope of 46 mV dec^{-1}, which is slightly larger than that of the Pt plate (36 mV dec^{-1}), but much less than those of Ru@OALC (58 mV dec^{-1}) and FeNi@OALC (361 mV dec^{-1}), indicating faster reaction kinetics. Combined with the reaction path of HER in the alkaline solution and Tafel slope of Ru–FeNi@OALC, the Volmer–Heyrovsky path is the rate-determining step. Therefore, the initial adsorption of H_2O molecules was crucial for the subsequent process. Abundant defects and disorder might promote the adsorption of H_2O molecules and enhance the HER performance of Ru–FeNi@OALC. To gain deeper insight into the activity of Ru-FeNi@OALC, electrochemical impedance spectroscopy (EIS)

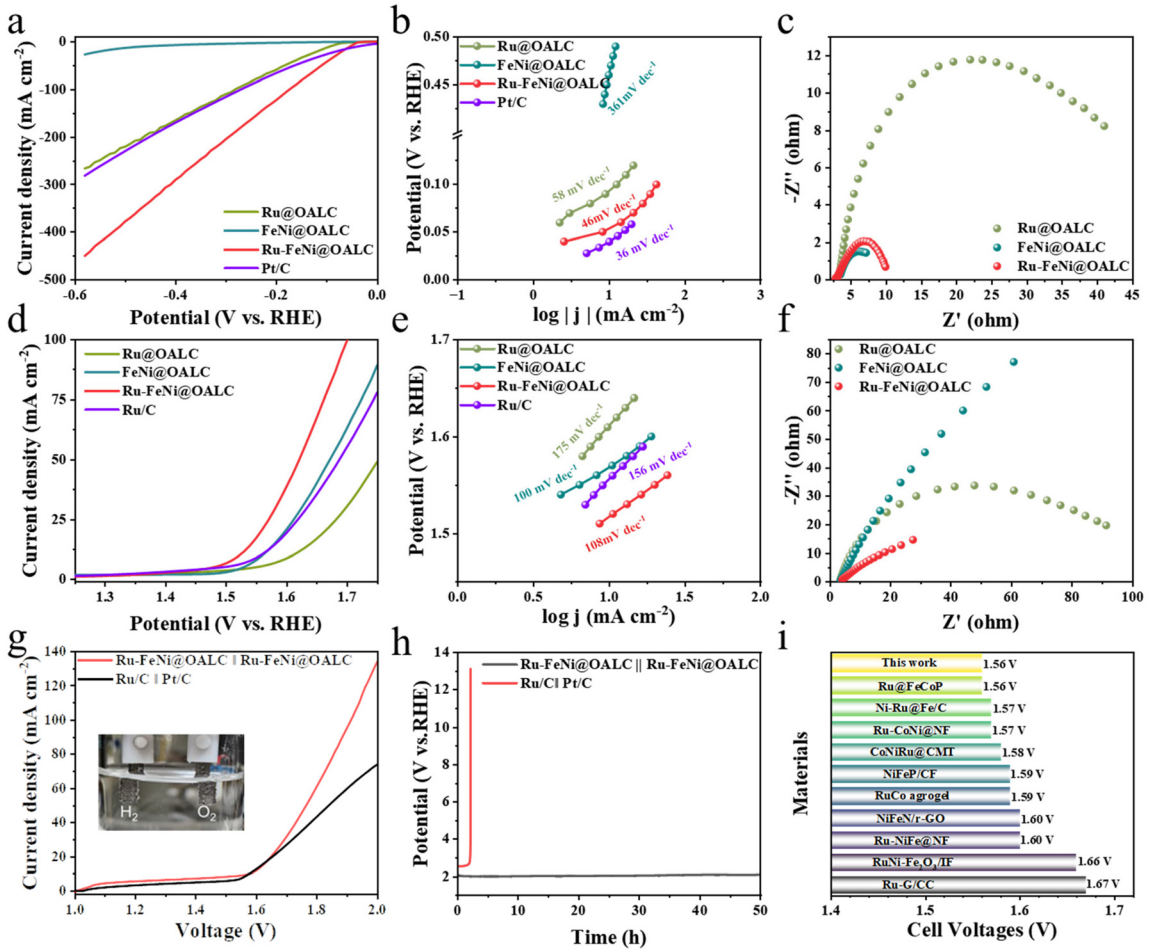

Fig. 5 The electrocatalytic activities of Ru–FeNi@OALC. (a) HER polarization curves. (b) HER Tafel plots. (c) HER electrochemical impedance spectroscopy (EIS). (d) OER polarization curves. (e) OER Tafel plots. (f) OER electrochemical impedance spectroscopy (EIS). (g) OWS polarization curves. (h) Time dependencies of the voltage of long-term OWS. (i) Comparison with OWS performances reported in the literature.

tests were performed. The resulting Nyquist plots are shown in Fig. 5c. The values of charge-transfer resistance (R_{ct}) of the catalysts were determined to be 38.73, 8.50, and 5.90 Ω for the Ru@OALC, FeNi@OALC, and Ru-FeNi@OALC catalysts, respectively. The smallest R_{ct} value of the Ru–FeNi@OALC catalyst suggests the fastest HER kinetics, which could be attributed to the synergistic effects of the FeNi alloy, Ru nanoparticles, and the lignin-derived carbon layer. Besides the high HER catalytic activity, Ru–FeNi@OALC also showed robust OER catalytic performance (Fig. 5d and e). The overpotential of Ru–FeNi@OALC to reach a current density of 10 mA cm^{-2} was about 290 mV, and the Tafel slope was 108 mV dec^{-1}, which were both superior to Ru@OALC (381 mV and 175 mV dec^{-1}), FeNi@OALC (338 mV and 100 mV dec^{-1}) and the commercial Ru/C catalyst (335 mV and 156 mV dec^{-1}). Besides, the overpotential of Ru–FeNi@OALC at high current density showed greater advantages. Besides, Ru–FeNi@OALC also displayed the lowest electrochemical impedance (54.8 Ω) during the OER process (Fig. 5f). The small Tafel slope and low electrochemical impedance meant that the current density could more quickly increase with the increase in the applied potential. This characteristic benefited industrialized application at the operating conditions of high voltage and large current density. These electrochemical behaviors further proved that the carrier could significantly affect the electrochemical activity of the HER and OER. Inspired by the excellent HER and OER performance of Ru–FeNi@OALC, we accordingly assembled a water-splitting device in 1.0 M KOH solution, whose anode and cathode were both composed of Ru–FeNi@OALC. Remarkably, as revealed in Fig. 5g, the overall water splitting required a low overpotential of 1.56 V to launch a current density of 10 mA cm^{-2}. Such a performance was superior to that of the Pt/C||Ru/C couple, and many reported bifunctional electrocatalysts (Fig. 5i and Table S7†). In addition, the stability test (Fig. 5h) showed no obvious degradation during the 50 h timescale at a current density of 100 mA cm^{-2}, while the noble metal-based electrolysis cell lost its activity after only 3 h of electrolysis. The protective mechanism of the lignin-derived carbon layer kept Ru–FeNi@OALC from being destroyed during the catalytic process. The corresponding TEM image showed that the original active sites and defects were maintained after the stability test (Fig. S8†). In

addition, no obvious changes were observed in the XPS spectra (Fig. S9†), which demonstrated the long-term stability of Ru–FeNi@OALC during the stability tests.

The changes of Ru–FeNi@OALC in the HER and OER processes were characterized by *in situ* Raman spectroscopy. In the process of Ru–FeNi@OALC catalytic water electrolysis, the peristaltic pump ensured the circulating flow of electrolyte in the sample cavity and inhibited the influence of bubbles on Raman spectrum acquisition during the reaction process. In the HER process (Fig. 6a), the Raman bands near 1135 cm^{-1} and 1524 cm^{-1} could be attributed to the vibrations of the Ru–H bonds adsorbing hydrogen (*H) on the surface of metal Ru (0) and water at the interface, respectively. With the increase in potential, the vibration frequency of the Ru(n^+)–H Raman band near 1135 cm^{-1} and 1524 cm^{-1} was redshifted, and the intensity decreased gradually, which might be caused by the gradual reduction of high-valence Ru(n^+) to zero valence Ru(0) under the reduction potential.[59] It is worth mentioning that in the initial state, the catalyst surface contained different valence states of Ru. In the range of the HER potential, hypervalent Ru was reduced continuously, and its surface behavior was affected by potential-induced changes and time-history changes. The relative strength ratios of the D and G bands of carbonaceous materials at 1327 cm^{-1} and 1563 cm^{-1} were basically unchanged. In the OER process (Fig. 6b), the peak at 810 cm^{-1} was attributed to the asymmetric stretching pattern of oxygen in binding the O–M–O bond (M = FeNi alloy), and MOO^- was a critical oxygen intermediate in the OER process.[60,61] As the potential increased, the reaction became more intense, reaching saturation at 1.7 V. In addition, I_D/I_G increased with the applied potential, indicating that defective carbon also participated in the OER process through the formation and desorption of adsorption reactants and intermediates at different stages of the OER process. With the increase in defects, the electron transport ability of lignin-derived carbon was gradually enhanced, and the interaction between carbon defects and active substances was also enhanced. *In situ* Raman results also showed that HER activity was derived from Ru and OER activity was derived from the FeNi alloy.

To better understand the higher HER and OER activities of Ru–FeNi@OALC, detailed HER and OER mechanisms have been investigated using DFT calculations. The OER process

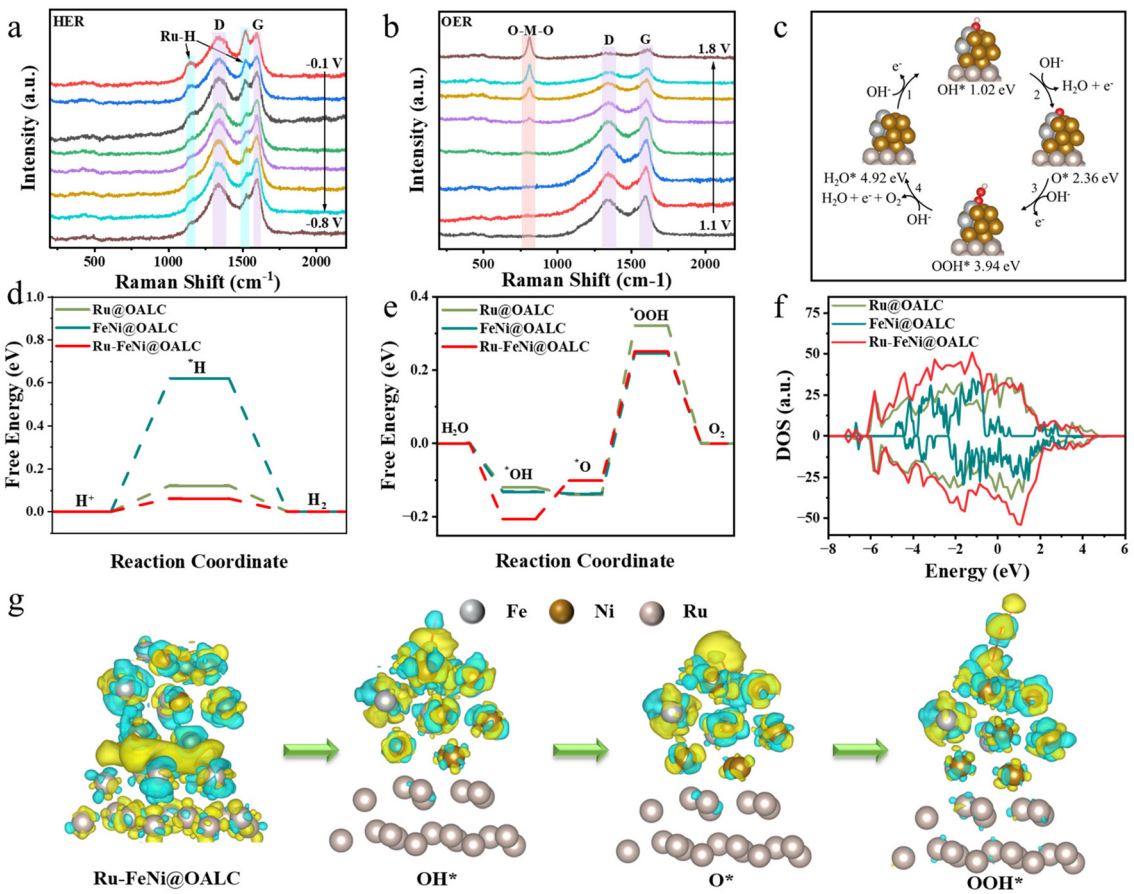

Fig. 6 *In situ* Raman spectra collected on Ru–FeNi@OALC for (a) the HER process and (b) the OER process in 1.0 M KOH solution. Catalytic activity evaluated by DFT simulation: (c) proposed reaction circle with geometry-optimized intermediates for the OER and HER over the Ru–FeNi@OALC catalyst; (d and e) Gibbs free energy for the HER and OER; (f) the DOS results during the DFT calculations; (g) charge density difference in intermediates for the OER and HER over the Ru–FeNi@OALC catalyst.

can be summarized in a $4e^-$ transfer mode in an alkaline solution (Fig. 6c), where * represents an active site on the catalyst surface, and OH*, O*, and OOH* are the oxygen intermediates. These results indicated that the rate-determining step of the OER process on FeNi@OALC was the formation of *OOH, and the free energy (ΔG) was 1.612 eV (Fig. S10†), illustrating strong interaction with HO* and O* species, leading to a marked uphill formation for the subsequent OOH* intermediate. For Ru–FeNi@OALC, ΔG at the FeNi sites adjacent to the Ru nanoparticle decreased to 1.58 eV, which suggests that the heterointerface created by the Ru and FeNi alloy is able to lower the overpotential at the FeNi sites and further promote electrocatalytic activity for the OER, thus resulting in entirely improved catalytic performance. Similarly, regarding HER, the RDS of the Ru–FeNi heterostructure becomes the hydrogen adsorption step with a ΔG_{*H} value of 0.06 eV, which is superior to that of the Ru@OALC (0.12 eV) and FeNi@OALC (0.62 eV) limited by the hydrogen desorption step (Fig. 6d and e). The DOS results during the DFT calculations (Fig. 6f) show that the DOS of Ru–FeNi@OALC had more orbital overlap above the Fermi energy level compared with that of Ru@OALC and FeNi@OALC, which enhanced the orbital hybridization between the catalyst and surface reaction intermediates, forming more antibonding orbitals and reducing the HER and OER reaction energy barriers. The charge density difference reveals that the establishment of the Ru–FeNi heterostructure could markedly induce charge density redistribution (Fig. 6g and S11†). A large number of electrons assemble at the heterointerface between the Ru and FeNi layers, resulting in higher electronic states near the Fermi level relative to independent Ru and FeNi. This indicates enhanced electronic conductivity for the Ru–FeNi heterostructure, which is conducive to accelerating electron transfer during the electrocatalytic process.

4 Conclusions

In summary, we propose a local lignin–metal supramolecular framework strategy to simply prepare highly efficient catalysts with ultra-small particle size and high dispersion for electrocatalytic water decomposition reactions based on the specific spatial limiting effect of the coordination process. Structural measurements of the supramolecular precursor suggest that metal ions possess unprecedentedly high dispersity, which greatly exceeds that of previously reported lignin-derived electrocatalysts. The as-prepared catalyst Ru–FeNi@OALC demonstrates an overwhelming advantage over the state-of-the-art Ru/C electrode and Pt/C benchmark catalyst. Experimental mechanism investigations combined with DFT calculations suggest that the reaction proceeds in higher electronic states near the Fermi level, relative to independent Ru and FeNi, which facilitates specific OER and HER performance during the subsequent water-splitting process. This work represents a significant advancement in developing high-performance and cost-effective catalysts from lignin and valorization *via* green and sustainable electrocatalyst preparation. Additionally, by utilizing the unique characteristics of lignin and acylamide functional groups, the proposed lignin modification method holds significant development potential across multiple fields, including heavy metal recovery, bioanalytical texting, polymer modification, and slow-release organic fertilizers.

Conflicts of interest

The authors declare no competing interests.

Acknowledgements

The authors acknowledge the financial support of the National Natural Science Foundation of China (U23A6005, 22178069, 22038004, and 22208061).

References

1 C. Lei, S. Lyu, J. Si, B. Yang, Z. Li, L. Lei, Z. Wen, G. Wu and Y. Hou, *ChemCatChem*, 2019, **11**, 5855–5874.
2 J. Mohammed-Ibrahim and X. Sun, *J. Energy Chem.*, 2019, **34**, 111–160.
3 J. Wang, J. Kim, S. Choi, H. Wang and J. Lim, *Small Methods*, 2020, **4**, 2000621.
4 Y. Zhu, W. Zhou and Z. Shao, *Small*, 2017, **13**, 1603793.
5 J. Mohammed-Ibrahim, *J. Power Sources*, 2020, **448**, 227375.
6 I. K. Sideri and N. Tagmatarchis, *Chem. – Eur. J.*, 2020, **26**, 15397–15415.
7 S. R. Ede and Z. Luo, *J. Mater. Chem. A*, 2021, **9**, 20131–20163.
8 X. Xie, L. Du, L. Yan, S. Park, Y. Qiu, J. Sokolowski, W. Wang and Y. Shao, *Adv. Funct. Mater.*, 2022, **32**, 2110036.
9 Y. Yang, J. Su, P. Jiang, J. Chen, L. Hu and Q. Chen, *Chin. J. Chem.*, 2021, **39**, 2626–2637.
10 F. Zoller, S. Häringer, D. Böhm, J. Luxa, Z. Sofer and D. Fattakhova-Rohlfing, *Small*, 2021, **17**, 2007484.
11 M. Zhang, J. Zhang, S. Ran, W. Sun and Z. Zhu, *Electrochem. Commun.*, 2022, **138**, 107283.
12 A. S. Souza, L. S. Bezerra, E. S. F. Cardoso, G. V. Fortunato and G. Maia, *J. Mater. Chem. A*, 2021, **9**, 11255–11267.
13 D. M. Morales, M. A. Kazakova, S. Dieckhöfer, A. G. Selyutin, G. V. Golubtsov, W. Schuhmann and J. Masa, *Adv. Funct. Mater.*, 2020, **30**, 1905992.
14 S. Ohn, S. Y. Kim, S. K. Mun, J. Oh, Y. J. Sa, S. Park, S. H. Joo, S. J. Kwon and S. Park, *Carbon*, 2017, **124**, 180–187.
15 J. Li, Z. Meng, D. J. L. Brett, P. R. Shearing, N. T. Skipper, I. P. Parkin and S. Gadipelli, *ACS Appl. Mater. Interfaces*, 2020, **12**, 42696–42703.
16 X.-Z. Li, L.-P. Zhou, L.-L. Yan, Y.-M. Dong, Z.-L. Bai, X.-Q. Sun, J. Diwu, S. Wang, J.-C. Bünzli and Q.-F. Sun, *Nat. Commun.*, 2018, **9**, 547.

17 I. V. Kolesnichenko and E. V. Anslyn, *Chem. Soc. Rev.*, 2017, **46**, 2385–2390.
18 G. Zhang, H. Wang, X. Deng, Y. Yang, T. Zhang, J. Wang, H. Zeng, C. Wang and Y. Deng, *Chem. Eng. J.*, 2021, **413**, 127525.
19 J. Liu, L. Chen, H. Cui, J. Zhang, L. Zhang and C.-Y. Su, *Chem. Soc. Rev.*, 2014, **43**, 6011–6061.
20 M. Renom-Carrasco and L. Lefort, *Chem. Soc. Rev.*, 2018, **47**, 5038–5060.
21 Y. Liu, Z. Liu, J. Jia, G. Ye, Y. Xie, W. Wang, J. Chen, T. Hu and K. Matyjaszewski, *Chem. Mater.*, 2022, **34**, 3525–3535.
22 M. A. Rahim, M. Björnmalm, T. Suma, M. Faria, Y. Ju, K. Kempe, M. Müllner, H. Ejima, A. D. Stickland and F. Caruso, *Angew. Chem., Int. Ed.*, 2016, **55**, 13803–13807.
23 H. Liang, B. Zhou, D. Wu, J. Li and B. Li, *Adv. Colloid Interface Sci.*, 2019, **272**, 102019.
24 C. Park, B. J. Yang, K. B. Jeong, C. B. Kim, S. Lee and B.-C. Ku, *Angew. Chem., Int. Ed.*, 2017, **56**, 5485–5489.
25 D. Payra, Y. Yamauchi, S. Samitsu and M. Naito, *Chem. Mater.*, 2018, **30**, 8025–8033.
26 K. C. Bentz and S. M. Cohen, *Angew. Chem., Int. Ed.*, 2018, **57**, 14992–15001.
27 Z. Chen and V. W.-W. Yam, *Angew. Chem., Int. Ed.*, 2020, **59**, 4840–4845.
28 W. Lan, M. T. Amiri, C. M. Hunston and J. S. Luterbacher, *Angew. Chem., Int. Ed.*, 2018, **57**, 1356–1360.
29 Q. Meng, J. Yan, R. Wu, H. Liu, Y. Sun, N. Wu, J. Xiang, L. Zheng, J. Zhang and B. Han, *Nat. Commun.*, 2021, **12**, 4534.
30 J. D. Nguyen, B. S. Matsuura and C. R. J. Stephenson, *J. Am. Chem. Soc.*, 2014, **136**, 1218–1221.
31 M. Rafiee, M. Alherech, S. D. Karlen and S. S. Stahl, *J. Am. Chem. Soc.*, 2019, **141**, 15266–15276.
32 Y. She, X. Li, Y. Zheng, D. Chen, X. Rui, X. Lin and Y. Qin, *Energy Environ. Mater.*, 2024, **7**, e12538.
33 W. Wu, Z. Luo, B. Liu, X. Qiu, J. Lin, S. Sun, X. Wang, X. Lin and Y. Qin, *Small Methods*, 2023, **7**, 2300462.
34 Y. Qi, B. Liu, X. Qiu, X. Zeng, Z. Luo, W. Wu, Y. Liu, L. Chen, X. Zu, H. Dong, X. Lin and Y. Qin, *Adv. Mater.*, 2023, **35**, 2208284.
35 S. Bertella and J. S. Luterbacher, *Trends Chem.*, 2020, **2**, 440–453.
36 M. Österberg, M. H. Sipponen, B. D. Mattos and O. J. Rojas, *Green Chem.*, 2020, **22**, 2712–2733.
37 A. d. E. S. Pereira, J. Luiz de Oliveira, S. Maira Savassa, C. Barbara Rogério, G. Araujo de Medeiros and L. F. Fraceto, *J. Cleaner Prod.*, 2022, **345**, 131145.
38 X. Lin, P. Wang, R. Hong, X. Zhu, Y. Liu, X. Pan, X. Qiu and Y. Qin, *Adv. Funct. Mater.*, 2022, **32**, 2209262.
39 T. Li, Y. Yin, S. Wu and X. Du, *Bioresour. Technol.*, 2022, **343**, 126120.
40 A. Moreno, J. Liu, R. Gueret, S. E. Hadi, L. Bergstrçm, A. Slabon and M. H. Sipponen, *Angew. Chem., Int. Ed.*, 2021, **60**, 20897–20905.
41 L. Jianglin, W. Linjun, C. Dalang, X. Quanzhou, C. Liheng, L. Xuliang and Q. Yanlin, *Chem. Eng. Sci.*, 2024, **285**, 119596.
42 C. Dalang, L. Jianglin, Q. Xueqing, L. Bowen, W. Xiaofei, Q. Zhongjie, L. Xuliang and Q. Yanlin, *AIChE J.*, 2024, **70**, e18323.
43 K. Shikinaka and Y. Otsuka, *Green Chem.*, 2022, **24**, 3243–3249.
44 M. H. Sipponen, H. Lange, C. Crestini, A. Henn and M. Österberg, *ChemSusChem*, 2019, **12**, 2039–2054.
45 X. Wang, X. Liu, R. L. Smith, Y. Liang and X. Qi, *Green Chem.*, 2021, **23**, 8632–8642.
46 H. Liu, Q. An, J. Kim, L. Guo, Y. Zhao, Z. Xiao and S. Zhai, *J. Hazard. Mater.*, 2020, **391**, 122253.
47 X. Lin, X. Fei, D. Chen, Y. Qi, Q. Xu, Y. Liu, Q. Zhang, S. Li, T. Wang, Y. Qin and X. Qiu, *ACS Catal.*, 2022, **12**, 11573–11585.
48 Z. Jinhui, L. Jianglin, L. Bowen, L. Xuliang and Q. Yanlin, *Chem. Eng. Sci.*, 2023, **280**, 119049.
49 L. Xuliang, L. Jianglin, W. Linjun, C. Liheng, Q. Yi, Q. Zhongjie, S. Shirong, D. Huafeng, Q. Xueqing and Q. Yanlin, *AIChE J.*, 2022, **68**, e17785.
50 X. Lin, J. Liu, X. Qiu, B. Liu, X. Wang, L. Chen and Y. Qin, *Angew. Chem., Int. Ed.*, 2023, **62**, e202306333.
51 C. Chio, M. Sain and W. Qin, *Renewable Sustainable Energy Rev.*, 2019, **107**, 232–249.
52 J. L. Espinoza-Acosta, P. I. Torres-Chávez, J. L. Olmedo-Martínez, A. Vega-Rios, S. Flores-Gallardo and E. A. Zaragoza-Contreras, *J. Energy Chem.*, 2018, **27**, 1422–1438.
53 R. Trovagunta, T. Zou, M. Österberg, S. S. Kelley and N. Lavoine, *Carbohydr. Polym.*, 2021, **254**, 117480.
54 M. Gigli and C. Crestini, *Green Chem.*, 2020, **22**, 4722–4746.
55 S. Sun, T. Akiyama, T. Yokoyama and Y. Matsumoto, *J. Agric. Food Chem.*, 2020, **68**, 6819–6825.
56 S. Sun and T. Yokoyama, *J. Wood Sci.*, 2021, **67**, 29.
57 S. Sun, X. Qiu, S. Hao, S. Ravichandran, J. Song and W. Zhang, *Green Chem.*, 2023, **25**, 3127–3136.
58 L. Li, C. Tang, Y. Zheng, B. Xia, X. Zhou, H. Xu and S. Z. Qiao, *Adv. Energy Mater.*, 2020, **10**, 2000789.
59 X. Chen, X.-T. Wang, J.-B. Le, S.-M. Li, X. Wang, Y.-J. Zhang, P. Radjenovic, Y. Zhao, Y.-H. Wang, X.-M. Lin, J.-C. Dong and J.-F. Li, *Nat. Commun.*, 2023, **14**, 5289.
60 Y. Liu, Z. Chen, Z. Li, N. Zhao, Y. Xie, Y. Du, J. Xuan, D. Xiong, J. Zhou, L. Cai and Y. Yang, *Nano Energy*, 2022, **99**, 107325.
61 Z. Na, G. Shi-Xian, Z. Qing, Z. Jia-Rong, Z. Jian-Yong, K. Qin-Fei and F. Yong-Zheng, *Chem. Eng. J.*, 2023, **65**, 103086.